Cyclic plasticity and damage mechanisms of Ti-6Al-4V processed by electron beam melting

A.K. Syed [a,*], D. Parfitt [a], D. Wimpenny [b], E. Muzangaza [b], B. Chen [a,c,*]

[a] *Faculty of Engineering, Environment and Computing, Coventry University, Coventry CV1 5FB, UK*
[b] *The Manufacturing Technology Centre Ltd, Pilot Way, Ansty Park, Coventry CV7 9JU, UK*
[c] *School of Engineering, University of Leicester, Leicester LE1 7RH, UK*

A B S T R A C T

Cyclic deformation and damage mechanisms in electron-beam-melted Ti-6Al-4V are investigated. As-built samples exhibit a graded microstructure over the height of 120 mm, with samples from the top having larger α-laths and higher plastic strain. After HIPing, the α-lath width is greater, with reduced grain misorientation, and lower microstructural and property gradients. In both conditions, the observed cyclic softening is dominated by a monotonic reduction in the friction stress and an increase in grain misorientation, suggesting the lath structure progressively fragments into smaller grains. As-built samples show typically lower fatigue life due to crack initiation from gas pores and lack-of-fusion defects.

1. Introduction

Electron beam melting (EBM) of Ti-6Al-4V (referred as Ti64 hereafter) is a powder-bed-fusion additive manufacturing (AM) method that is rapidly maturing for load-bearing structural applications, and hence understanding the fatigue behaviour is important. The microstructure and texture of AM materials differ considerably from those in wrought and cast products. A lack of fundamental understanding about their cyclic plasticity and damage mechanisms has become a concern [1]. In the as-built condition, high-cycle fatigue (HCF, $>10^4$ cycles) of EBM Ti64 is influenced by surface roughness [1]. If the roughness is reduced, process-inherent gas pores or lack-of-fusion defects, which originate either from entrapped gas or insufficient powder consolidation, become the life-limiting factor [1,2]. Defects that are large and close to the surface are more detrimental to fatigue life [2,3]. A similar concern exists in laser powder-bed-fusion (LPBF) Ti64 [4] which has a cooling rate typically two orders of magnitude faster than EBM. This rapid cooling favours the formation of α' martensite [5,6] compared to the fully homogenised α + β microstructure typically found in EBM Ti64. Despite the different microstructures, the fatigue life of EBM and LPBF Ti64 are similar [7], suggesting that defects are dominant under HCF loading.

Ti64 subjected to low-cycle fatigue (LCF, $<10^4$ cycles) typically experiences cyclic softening [8] and the plastic deformation is controlled predominantly by the high-volume fraction (90 to 95%) of α-phase [8]. Plastic deformation of Ti64 is accommodated by a complex mixture of dislocation slip and twinning [9,10]. When considering the LCF performance, limited data is available for AM Ti64. Agius et al. [11] investigated the microstructural anisotropy and the cyclic elastoplastic behaviour of LPBF Ti64. An asymmetric softening characterised by a vertical (i.e., stress) shift in the hysteresis loop under symmetric strain loading was observed. Agius et al. claimed that the anisotropic plasticity was attributed to the considerable thermal residual stresses induced by the fast-cooling rate of 10^5 K/s, which in turn led to asymmetric cyclic yield, effective and back stresses when subjected to compression and tension phases [11]. This seemed to provide a reasonable explanation for the progressively diminished role of residual stresses with increased fatigue cycling. The effect of residual stresses on cyclic properties of LPBF Ti64 were previously reported. Simonelli et al. [12] experimentally studied the effect of build orientation on residual stresses and mechanical performance in LPBF Ti64. Regardless of the build orientation, a tensile residual stress of ∼ 250 MPa was measured in the as-built condition that contributed to the poor elongation at failure. In another laser-based AM work, Ren et. al [13] studied the LCF of Ti64 processed by blown powder directed laser deposition (DLD) in the heat treated condition. By comparison with the wrought Ti64, the LCF performance of DLD Ti64 was found to be lower at low strain amplitudes (<1.1%), while being similar at higher strain amplitudes. The presence of surface

---

defects as small as 60 μm were claimed to be detrimental to the LCF [13].

As opposed to LPBF, the process temperature in EBM is higher (>700 °C) [7], due to powder layer preheating. This will lead to lower cooling rates and negligible residual stresses. However, the typical thermal cycles of preheating, melting and rapid solidification as well as the large thermal gradients along the build direction in EBM are known to produce microstructural gradients [14–16]. The α-lath width in wrought Ti64 is the primary microstructural scale parameter that controls mechanical properties [17,18]. Recent studies in EBM Ti64 reported a graded microstructure where both the α-lath and primary β-grain widths increased along the build direction [19–22], resulting in tensile properties and hardness variation from the bottom to top of the build. Hitesh et al. [21] correlated the decrease in micro-hardness from 406 to 382 HV to the increase in mean α-lath width from 0.58 ± 0.24 μm to 0.87 ± 0.33 μm. Tan et al. [22] observed a similar microstructure gradient but on a shorter EBM sample and attributed it to the cooling rate gradient. Both groups [21,22] correlated the change in hardness to the α-lath width using a Hall-Petch relation. In another study [23], the influence of build thickness on microstructure and mechanical properties was investigated. The microstructure of thin deposits consisted of a brittle α′ martensite while a ductile α + β phase was found in thicker deposits. The microstructure in the thicker deposits was attributed to the prolonged high-temperature exposure and lower cooling rate. Nevertheless, the influence of graded microstructure on cyclic deformation and damage processes in EBM Ti64 has yet to be explored.

One way to overcome the concerns over the influence of defects and graded microstructure is to subject the EBM materials to post processing treatments. Hot isostatic pressing (HIPing) for example will increase the densification and homogenisation [2,4,24] and can increase the fatigue strength by twofold compared to the as-built condition [24]. In conjunction with the cyclic plasticity of as-built Ti64, a deeper understanding is required of the persistence of the graded microstructure after HIPing and to assess its potential impact on LCF behaviour. Such information is not only important for engineering applications, but also provides underlying data for elastoplastic constitutive models so that mechanistic-based fatigue life predictions can be developed. The present paper aims to fill in the above-mentioned research gaps in EBM Ti64.

This has been achieved by (i) investigating the influence of HIPing on the graded microstructure and (ii) comparing the LCF cyclic deformation and damage process in the as-built and HIPed conditions.

2. Material and experimental

2.1. Sample fabrication

Two rectangular plates with a width of 100 mm, thickness of 15 mm and total build height of 120 mm (Fig. 1a) were produced in an Arcam Q20 plus system using a standard Arcam build theme for Ti-6Al-4V with control software version 5.0. They were built using a layer thickness of 90 μm and accelerating voltage of 60 kV. The detailed processing parameters can be found elsewhere [21]. One EBM plate was subjected to HIPing at 920 °C under 100 MPa pressure for 2 h, followed by cooling in the furnace at a rate between 6 and 12 °C/min to ambient temperature. Both plates were built using the Arcam gas atomised Ti64 powder (Grade 5) in recycled condition. Fig. 1b shows the powder particle size distribution and its typical morphology. The chemical compositions of the powder, as-built and HIPed samples are presented in Table 1. The inert gas fusion method (ASTM E1409) was used to measure the O and N contents while plasma spectroscopy (ASTM E2371) was used to measure the other elements. Little difference was found between the as-built and HIPed samples, except for the Al loss that can be attributed to the light element evaporation that is well known for the EBM process [25].

2.2. Material characterisation

Six samples were extracted along the build direction at different Z-

Table 1
Chemical compositions (wt%) of Ti64 powder and EBM built samples.

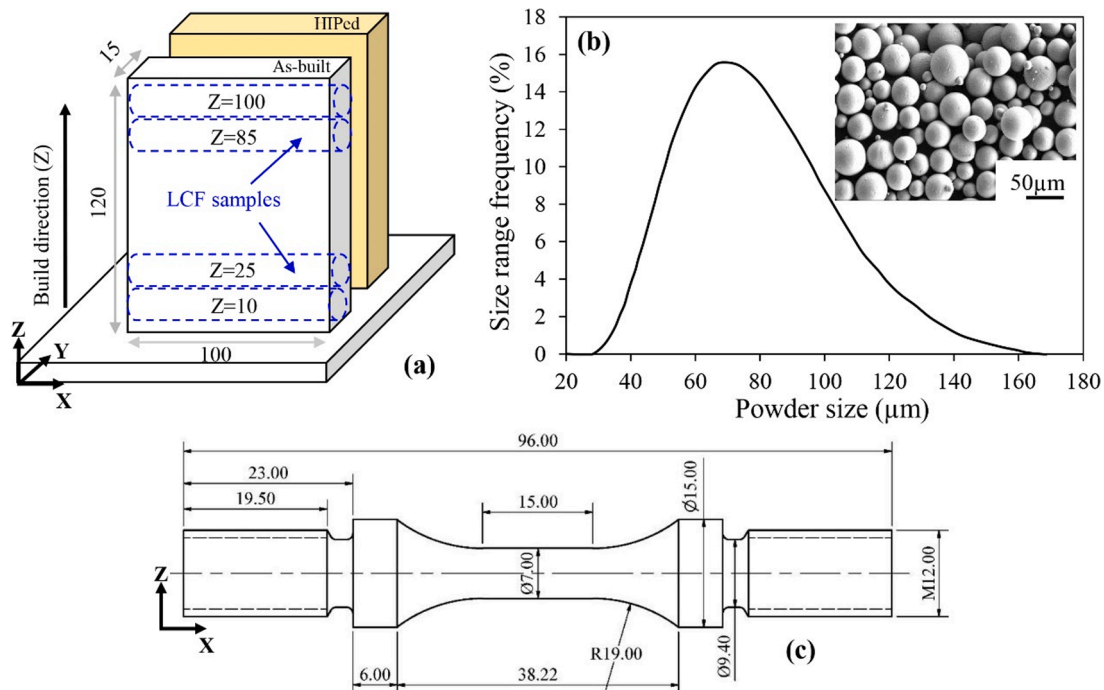| Sample ID	Al	Fe	N	O	V	Ti
Reused powder [21]	6.52	0.17	0.029	0.19	4.12	Bal.
As-built [21]	5.65	0.18	0.029	0.12	4.39	Bal.
HIPed	5.64	0.18	0.029	0.11	4.39	Bal.

Fig. 1. (a) Schematic of EBM built Ti64 plates showing the low-cycle fatigue (LCF) sample extraction plan at different build height of Z = 10, 25, 85 and 100 mm, (b) powder particle size distribution and SEM image showing the spherical shaped morphology [21]. (c) LCF specimen dimensions (all in mm).

build heights of 10, 60 and 100 mm, respectively, for microstructure examination on the X-Z plane, three each in the as-built and HIPed conditions. For metallography preparation, samples were ground using SiC papers down to 2500-grit, polished using diamond suspension down to 1 μm, and finished with the OPS polishing with colloidal silica of 0.02 μm. Some polished samples were etched with Kroll's reagent for ~ 45 s. A Zeiss Gemini Sigma 500VP scanning electron microscope (SEM) was used for quantitative microstructural analysis. For determining the α-lath width from approximately 300 measurements per sample condition, a statistical approach was chosen as reported elsewhere [21]. The α-lath width was defined by the distance between two neighbouring β-rods. Vickers micro-hardness measurements were performed using a 0.5 kgf load (HV0.5) for 10 s.

Micro-texture analysis was performed using electron backscattered diffraction (EBSD) on the as-built and HIPed samples from Z = 10 and 100 mm, representing the bottom and top of the build, respectively, before and after the LCF deformation. All EBSD scans were acquired at an accelerating voltage of 20 kV and a beam current of 1.7nA with a step size of 0.3 μm across an area of 100 μm × 50 μm. An overall indexing rate of 95% and 90% was achieved for before and after LCF deformation. The non-indexed data points were automatically reassigned through iteration process to the crystallographic orientations belonging to their nearest neighbours.

2.3. Low-cycle fatigue testing

The LCF sample extraction location with reference to Z-build heights is indicated in Fig. 1a and the sample dimensions are presented in Fig. 1c. Four LCF samples were extracted for each condition (as-built vs. HIP): two from the bottom and the other two from the top. LCF testing was performed following ASTM E606 [26]. Prior to testing, the sample gauge section was polished using a 4000-grit SiC paper to achieve a mirror polished surface finish, with a surface roughness of 0.2 μm as determined by using Bruker Interferometer. The LCF tests were performed at room temperature at a strain rate of 10^{-3} s^{-1} and with a predetermined total strain amplitude of ± 1%. The strain was controlled using a 10 mm gauge extensometer. Sample alignment is crucial for LCF testing to avoid buckling in compression. According to the ASTM E1012-10 standard, the alignment was performed by using a sample fitted with eight linear strain gauges that were spaced at 90° intervals along its circumference. This allows for the correction of both the concentric and angular misalignment. During the test, load, strain, displacement, and number of cycles were collected. The sample was considered as failed when the maximum force (stress) dropped to zero i.e., sample completely failed. After failure, fracture surfaces were studied using SEM to understand the crack initiation and failure mechanism.

2.4. A modified data analysis algorithm

Data analysis of the cyclic stress–strain curves was performed to link the microstructure with macroscopic LCF properties. Under cyclic loading, Ti64 exhibits changes in both the back stress and the friction stress that collectively determine the onset and subsequent evolution of cyclic plasticity [27]. Various schemes [27–32] exist for classifying these stresses including the per cycle offset proof strength or the minimum point in the second derivative of the stress-stain data plot. Here, we adopt a modified version of the former method. The latter derivative-based method is conceptually appealing, but in practice we found significant numerical uncertainty when applied to sparse stress–strain data.

Fig. 2 shows an example single cycle dataset where the grey points indicate individual measurement points around the characteristic hysteresis loop. Also indicated on the plot are the various per cycle parameters: the modulus in tension and compression, the offset proof stress and the range of elastic and plastic stress. To represent a smooth functional response of the stress relationship, the Ramberg-Osgood function was fitted via the least-squares method to each separate compressive and
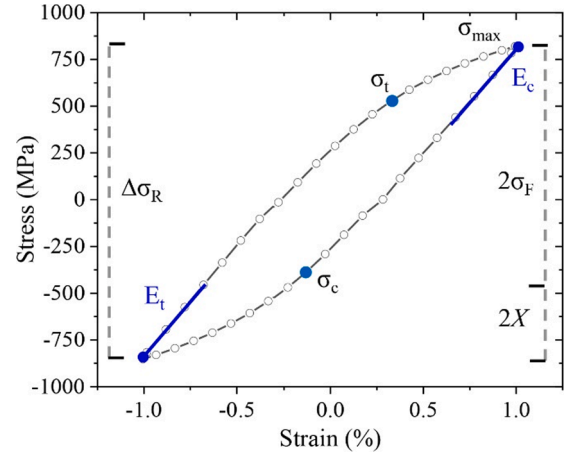

Fig. 2. Plot showing an example single cycle fatigue curve for the as-built Ti64. Grey points indicate the recorded fatigue data, while the dashed line is the Ramberg-Osgood fit.

tensile subset of the data, namely, the stress, σ, and strain, ε, in each half cycle are linked via:

$$\varepsilon = \varepsilon_{\text{elastic}} + \varepsilon_{\text{plastic}} = \frac{\sigma}{E_{\text{t,c}}} + \left(\frac{\sigma}{K}\right)^{1/n} \tag{1}$$

where $E_{\text{t,c}}$ are modulus values in tension (t) and compression (c), K is the cyclic strength coefficient and n is the cyclic strain hardening exponent. Fitting a curve of this nature is less sensitive to scatter in individual point measurements than the offset proof method applied to the original data. Thus, this method allows rapid evaluation of the per cycle proof strength at an arbitrary offset directly from Eq (1).

From the fitted Ramberg-Osgood relationship, the cycle response is further divided into an elastic stress range representing the difference between the points where the back stress is equal to the applied tensile or compressive stress, and a plastic stress range representing the subsequent deformation. There are different opinions in the literature over how best to define these ranges and the transition value between the two regimes. We assume the transition occurs at an offset plastic strain of 1 × 10^{-3} (for consistency with Ref. [27]); as shown in Fig. 2, a friction stress $2\sigma_{\text{F}} = \sigma_{\text{max}}$-$\sigma_c$ between the maximum stress during tension and the compressive offset stress σ_c that represents the elastic portion of the cyclic deformation can then be defined. Accordingly, the plastic stress range is then defined as $2X = \Delta\sigma_{\text{R}}$-$2\sigma_{\text{F}}$, where $\Delta\sigma_{\text{R}}$ is the applied stress range. The physical interpretation of these two values is that the friction stress (σ_{F}) represents the material isotropic hardening due for example to short-range interaction of dislocations with obstacles [33], while the back stress (X) represents the kinematic hardening due for example to strain incompatibilities between grains in a polycrystal [34], providing a long-range interaction with mobile dislocations.

3. Results and discussion

3.1. Microstructure gradient

The bulk microstructure of the as-built and HIPed Ti64 is characterised by columnar prior β-grains oriented along the build direction (Fig. 3a and 3b) and embedded α + β microstructure both in Widmanstätten and colony morphology (Fig. 3c and 3d). The columnar prior β-grains are the direct consequence of the steep thermal gradient and repeated heating and cooling cycles during the EBM. The as-built samples exhibit a finer microstructure (Fig. 3c) due to the martensitic transformation followed by transformation to Widmanstätten and colony α. The remaining β-phase has a rod and dot-like morphology embedded in the α-phase matrix. This is consistent with the previous
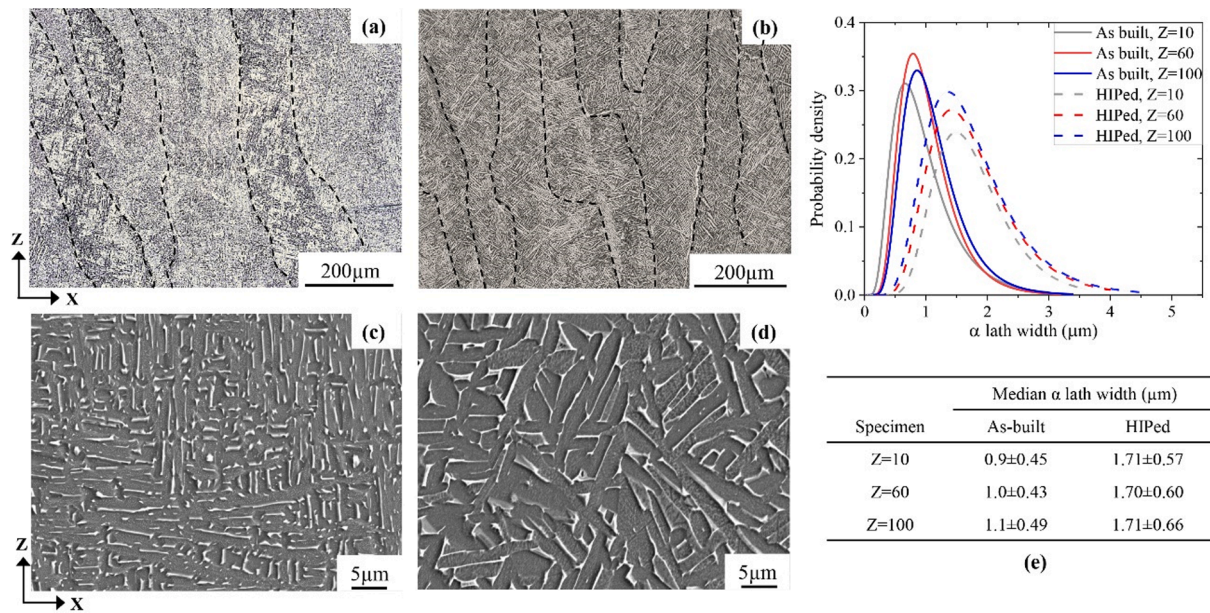
Fig. 3. Microstructures of the as-built in (a) and (c) and HIPed Ti64 in (b) and (d): (a) and (b) optical micrographs while (c) and (d) SEM micrographs. Dark and bright areas represent α and β phases under SEM imaging, respectively. (e) log-normal distribution plots of the measured α-lath width, together with the determined median α-lath width.

studies [22,35]. According to Shui et al. [35], such β-phase morphology is associated with the interface of the acicular microstructures. After HIPing at 920 °C (about 60 °C lower than the β-transus of 980 °C [36]), the columnar β-grains remain in the microstructure. Nevertheless, a considerable change in β-phase from the dot-like morphology to more continuous rod-like lamellar morphology can be seen in Fig. 3d. Also, α-laths continue to grow at the expense of neighbouring grains, causing an increase in the number of larger α-laths.

Fig. 3e presents log-normal distribution plots of the measured α-lath width at different Z-build heights. Such plot provides a better presentation of the measurement results because of the considerably large size difference in α-laths. Furthermore, we report the median α-lath width in the table of Fig. 3e, instead of the mean value, since it was proven to give better statistical description of the microstructure gradient in EBM Ti64 [21]. For the as-built condition, the median α-lath width at Z = 10, 60 and 100 mm was measured as 0.9 μm, 1.0 μm and 1.1 μm, respectively. It can be seen in Fig. 3e that the number of smaller α-laths at Z = 10 is higher than Z = 100, but the number of larger α-laths appears more frequently for the Z = 100 and Z = 60 when compared to Z = 10. The cooling rate is faster at the bottom of the build as the heat was conducted quickly through the substrate [20]. However, as the build height increased, it is difficult to quickly dissipate the heat due to the increased thermal resistance leading a slower cooling rate. As a result, a coarser microstructure is observed at the top of the build [20,22]. The microhardness was measured to be 346 ± 8 HV at Z = 10 while 327 ± 11 HV at Z = 100, and the lower hardness for the top can be attributed to the α-lath coarsening. After HIPing, there is virtually no difference between the top (322 ± 10 HV at Z = 100) and bottom (328 ± 8 HV at Z = 10) of the sample build. The hardness decrease in HIPed condition can be attributed to the increased α-lath width, with the median value being 1.71, 1.70 and 1.71 μm for Z = 10, 60 and 100 mm, respectively. HIPing helps to achieve a more homogeneous microstructure along the build direction of EBM Ti64.

3.2. Cyclic deformation behaviour

All the LCF data presented in this work were obtained by testing the EBM Ti64 under the same total strain amplitude of ± 1% and with the fatigue loading axis perpendicular to the build direction. The response of cyclic stress amplitude vs. number of cycles are presented in Fig. 4a and 4b for the as-built and HIPed samples, respectively. In general, a continuous cyclic softening behaviour is characterised by the progressive decrease in the applied stress amplitude (or peak tensile stress). The measured stress amplitude shows a continuous cyclic softening for both conditions that is consistent with that generally observed in wrought Ti64 [27]. The steep decrease in the stress amplitude on the far right of Fig. 4 manifests the rapid fatigue crack propagation leading to the final failure. Proper stress saturation was not reached in any of the samples; this applies to both the as-built and HIPed conditions. There was a slight surge in the stress amplitude at the 168th fatigue cycle for the Z = 25 mm sample in Fig. 4a. This was attributed to an unexpected increase in the peak compressive stress after examining the hysteresis loop at the corresponding cycle. The underlying reason for this is unclear and would require an in-situ study to clarify.

In the as-built condition, samples extracted from Z = 10 and 25 mm exhibit 2% higher peak stress compared to those of Z = 85 and 100 mm. The mechanical properties and the rate of plastic deformation in Ti64 depend on the size and morphology of the α- and β-phases, texture and defects [37]. In general, hexagonally close-packed (hcp) metals such as titanium alloys exhibit a reasonably strong Hall–Petch dependence as they have a large value of the Taylor factor [29]. To accommodate plastic strains, there is a need for slip occurring at grain boundaries on prismatic or pyramidal slip systems. The α-lath width and slip length are directly proportional and therefore the presence of smaller α-laths leads to a smaller slip length and more resistance to cyclic deformation. Thus, a higher stress is required to move the dislocation across the grains in as-built Z = 10 and 25 mm samples compared to the Z = 85 and 100 mm samples. By contrast, the HIPed samples show < 0.5% difference in the cyclic stress response, indicating much less dependency on the build height, Fig. 4b. This is as expected since a more homogenous microstructure was found after HIPing. Overall, the EBM Ti64 in HIPed condition has around 5% reduction in stress amplitude compared to the as-built samples.

Cyclic hysteresis loops at different fatigue cycles are shown in Fig. 5. A closer examination about the evolving tensile and compressive maximum stresses reveals two interesting phenomena. Firstly, when comparing the maximum stress for the 1st and stabilised cycles, it can be observed that the cyclic softening rate is higher in Z = 10 samples in
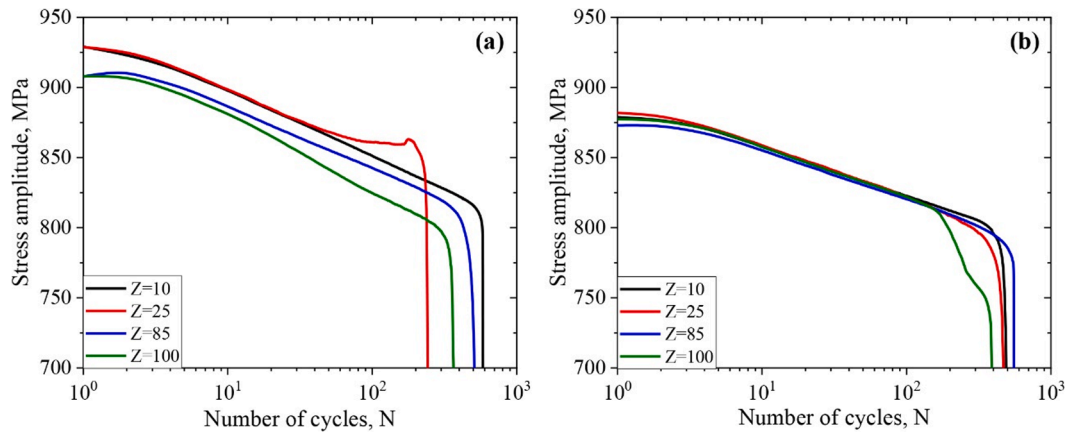
Fig. 4. Stress amplitude vs. number of cycles for (a) as-built and (b) HIPed Ti64 samples.
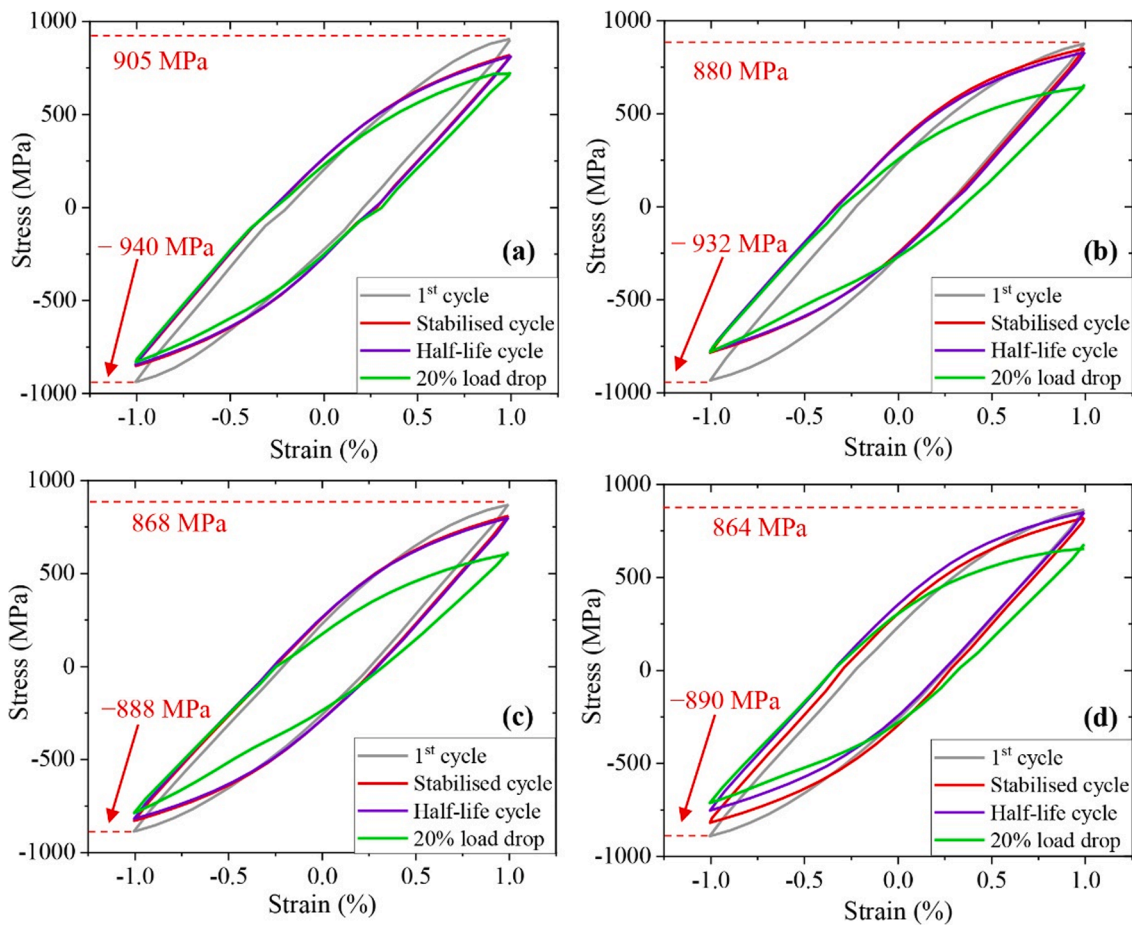

Fig. 5. Hysteresis loops at different number of cycles for as-built (a) Z = 10, (b) Z = 100 and HIPed samples (c) Z = 10, (d) Z = 100 mm.

both the as-built (Fig. 5a) and HIPed (Fig. 5c) conditions, whereas Z = 100 samples have lower softening rates (Fig. 5b and 5d). Secondly, all samples exhibit tension–compression asymmetry. In general, the maximum absolute tensile and compressive stresses are expected to progressively decrease during the cyclic softening. However, in the obtained results an asymmetric decrease in maximum absolute tensile and compressive stresses was found. It should be noted that, the asymmetry in tension and compression load causes increase in the stress ratio (i.e., the mean stress shifts towards the compression phase), despite all the samples tested in fully reversed loading under strain control of ± 1%. In other words, the effective stress ratio R is −1.03, instead of −1. In

addition, the difference between the absolute tensile and compressive stresses in the as-built Z = 10 sample is 35 MPa (Fig. 5a) whereas the stress difference is increased to 52 MPa for the Z = 100 (Fig. 5b), suggesting that the severity of the asymmetry is higher at the top of the build. Such gradient in severity of the asymmetry can also be linked to the graded microstructure. By comparison, the HIPed samples show a comparatively smaller stress difference, with 20 MPa for Z = 10 mm (Fig. 5c) while 26 MPa for Z = 100 mm (Fig. 5d). This seems to be consistent with the more homogeneous microstructure after HIPing.

Fig. 6 compares the cyclic softening rate of EBM Ti64 (present study) with its counterparts i.e., wrought Ti64 in the annealed condition
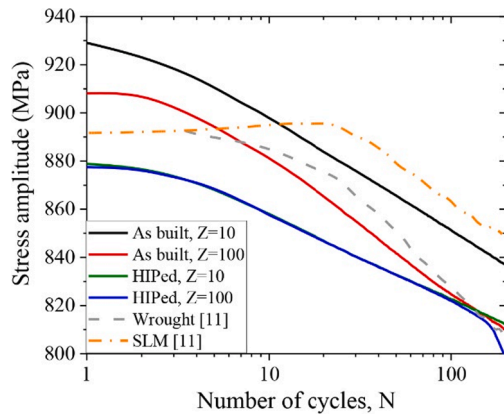
Fig. 6. A comparison of change in stress amplitude over the fatigue cycles for the as-built and HIPed Ti64 processed by EBM in the present work (solid lines) with the literature data [11].

consisting of globular α grains and SLM Ti64 with α' martensitic microstructure [11]. The cyclic softening rate depends on the applied strain amplitude and the microstructure [38]. An increase in strain amplitude led to increased rate of cyclic softening in wrought Ti64 with a bimodal microstructure [27]. Given that all the samples were tested under the same strain amplitude, any change in cyclic softening behaviour is due to the influence of microstructure. Compared to wrought and SLM Ti64, the EBM Ti64 in the as-built condition shows considerably higher peak stress. The higher yield strength in SLM Ti64 than the EBM counterpart [39], due to the presence of α' martensite and residual stresses in the former, is responsible for a lower cyclic peak stress when the specimen was tested under the same 1% strain amplitude. In addition, the stress amplitude is initially increased for the first 25 cycles and then decreased in SLM Ti64 showing initial cyclic hardening before the activation of cyclic softening [11]. The acicular α' phase has been shown to have high dislocation density [11,40], staking faults and twin structures, all of which will cause dislocation tangling at the α' grain boundaries leading to initial cyclic hardening in the first few cycles. As the fatigue cycles progress, the dislocation can move across the grain boundary and initiate cyclic softening. On the other hand, wrought Ti64 is composed of globular α which generally has a lower yield strength compared to EBM Ti64 [39]. As a result, a lower peak stress compared to EBM Ti64 for the same 1% strain amplitude is observed. Moreover, the absence of dislocation tangling characteristics also lead to a continuous cyclic softening in wrought material [11].

3.3. Stress partitioning based LCF data analysis

To further characterise the graded cyclic deformation behaviour, the plastic strain range was derived, for both the as-built and HIPed samples, based on the hypothesis that any change in the microstructure would cause a change in the accumulated cyclic plasticity. The plastic strain range was evaluated for the first cycle by using Ramberg-Osgood relation for cyclic stress, equation (1). The calculated plastic strain range values are presented in Table 2, where the graded cyclic plasticity can be

Table 2
Low-cycle fatigue (LCF) life and derived plastic strain range for the first cycle.

	As-built				HIPed			
	$Z = 10$	$Z = 25$	$Z = 85$	$Z = 100$	$Z = 10$	$Z = 25$	$Z = 85$	$Z = 100$
LCF life	590	250	538	374	593	504	558	412
Plastic strain range (%)	0.13	0.17	0.19	0.21	0.12	0.16	0.13	0.16

seen clearly for the as-built samples. Although the change in plastic strain between $Z = 10$ and 25 is smaller, a considerable change in plastic strain is found when the samples $Z = 10$ and 100 mm are compared. A 14% increase in median α-lath width from the bottom to the top of the build results in a 38% increase in plastic strain range. The plastic strain range increases due to the increase in effective dislocation slip length, in this case controlled by the α-lath width. To summarise, the EBM Ti64 not only shows a graded microstructure in the as-built condition but also shows a graded cyclic softening and plastic strain accumulation.

The friction stress (σ_F) and the back stress (X) extracted directly from the hysteresis loop, (as schematically shown in Fig. 2) is presented in Fig. 7. It is visible from Fig. 7a and 7b that with the increase of fatigue cycles, the friction stress shows a continuous decrease at a constant rate. On the other hand, the back stress presented in Fig. 7c and 7d remains approximately constant during the loading cycles. This indicates that the cyclic softening response as observed in our strain controlled LCF tests is driven by a monotonic reduction in the friction stress. Xu et al. [27] found a similar friction stress behaviour in wrought Ti64 and they identified the shearing of nanoscale Ti_3Al precipitates in Ti64 as the underlying mechanism. This agrees with our current knowledge about the per cycle friction stress as a measure of short-range interactions of dislocations with local obstacles, such as solute atoms or precipitates.

For the EBM Ti64 in the as-built condition, a variability in the absolute value of the friction stress (σ_F) can be seen in Fig. 7a, with the $Z = 10$ and $Z = 25$ samples having higher values than the $Z = 85$ and $Z = 100$ samples. This is likely due to the finer size of Ti_3Al precipitates in the lower Z-build regions subjected to a faster cooling rate when compared to the top. Future detailed microstructure characterisation work is needed to validate this hypothesis as the previous work was based on wrought Ti64 [27]. After HIPing, the EBM Ti64 shows a more uniform response with significantly reduced variability in the magnitude of friction stress, Fig. 7b. A closer observation of Fig. 7a reveals that the $Z = 10$ and 25 samples show marginally higher friction stress until approximately 100 cycles compared to $Z = 85$ and 100 samples, which is the evidence of gradient in isotropic hardening due to graded microstructure. On the other hand, such difference was not observed after HIPing.

As far as the back stress (X) is concerned, although it is not significantly varying with the increased fatigue cycles, again clear evidence indicating the influence of sample condition (as-built vs. HIPed) and the graded microstructure created by the EBM process can be observed. As-built samples (Fig. 7c) show a relatively higher back stress compared to HIPed samples (Fig. 7d) due to the shorter slip length and the probable pile-up of large number of geometrically necessary dislocations (GNDs) at the phase boundaries. For the as-built condition, the samples of $Z = 10$ and 25 show a higher back stress compared to those of $Z = 85$ and 100 (Fig. 7c) as a result of smaller α-lath width. Moreover, previous studies [41–43] have highlighted that the micro-mechanism of back stress in α + β Ti alloys is mainly linked to three different levels of heterogeneities in the materials. Firstly, difference in mechanical properties such as elastic modulus, yield strength etc. and thermal expansion coefficients between the two phases develop internal stresses [43]. Secondly, intergranular strain induced by the incompatibility or difference in two neighbouring α-phase grains [42–44]. Finally, the heterogeneous plastic deformation within single α-phase grain as a result of strain localisation, slip bands etc. In the current study, the β-phase fraction is significantly lower (<1%, as confirmed by the EBSD scan). Therefore, it can be considered that the dislocations movement and plastic deformation in β-phase is negligible. It is then assumed that the micro-mechanisms of deformation are mainly due to the α-phase. It is evident that the as-built samples of $Z = 10$ and 25 have smaller α-lath width than those of $Z = 85$ and 100 due to slower cooling rate with the Z-height increasing. As a result, the as-built samples of $Z = 10$ and 25 are associated with smaller slip length and higher intergranular strains. Such heterogeneity within the material resulted in higher back stress in the as-built $Z = 10$ than $Z = 100$ during the LCF tests. In the next section, we will seek the
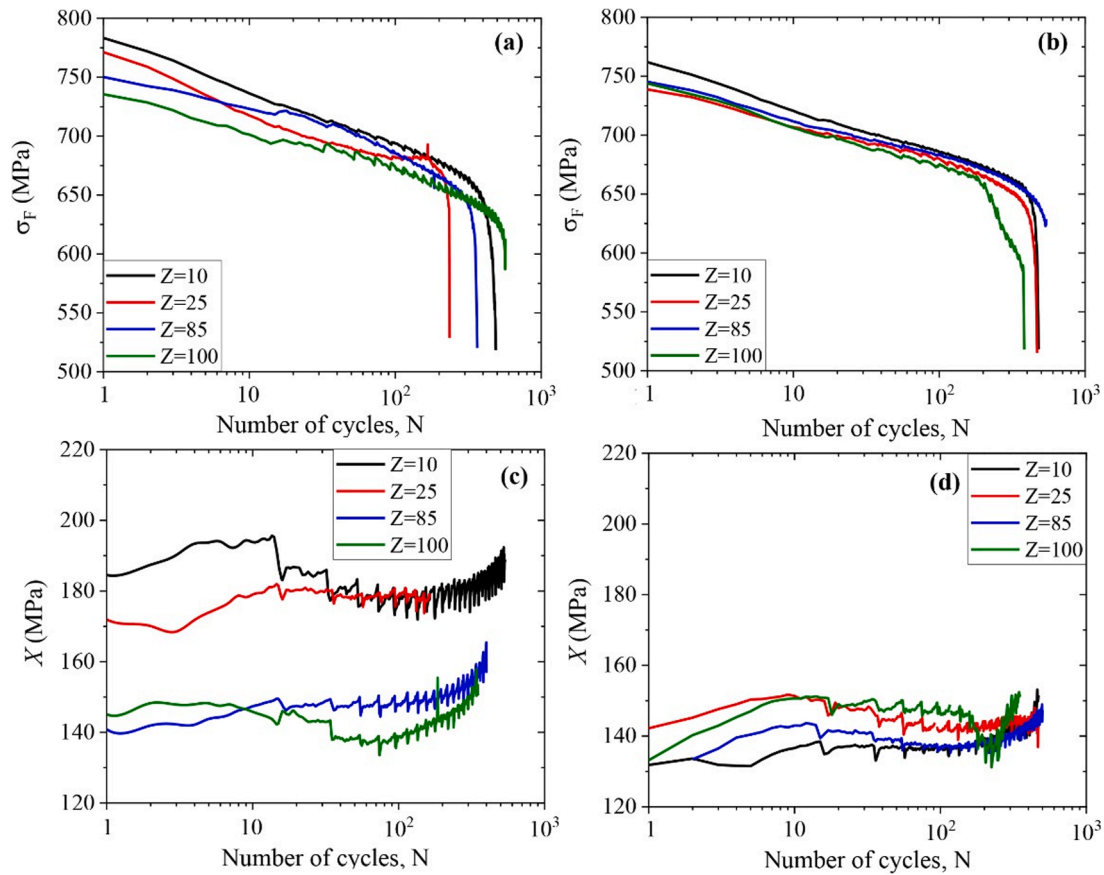
Fig. 7. Cyclic response of the as-built and HIPed samples from different Z-build heights showing the characteristic values of friction stress, σ_F, and back stress, X, as defined in Fig. 2: (a) and (c) as-built condition; (b) and (d) HIPed condition.

microstructure evidence to support the above discussions.

3.4. Cyclic deformation mechanisms and damage process

Fig. 8 shows EBSD inverse pole figure (IPF-Z) orientation maps and the corresponding frequency change in the grain misorientation angles from 0° to 5°. Based on the EBSD phase constitution determination, the α-phase proportion reduces slightly from 99% to 97% due to HIPing. The pole figure (not shown here for brevity) reveals the multiples of uniform density (mud) values as 12.16 and 15.31 for the Z = 10 and Z = 100 samples in the as-built condition, and 11.75 and 14.50 after HIPing. HIPing therefore does not dramatically change the texture. The mud levels for the LCF deformed microstructure were measured to be 12.4 (Z = 10) and 15.63 (Z = 100) for the as-built samples while 10.71 (Z = 10) and 8.41 (Z = 100) for the HIPed samples. After the LCF deformation, the grain size at and close to the fracture surface is evidently smaller than the region away from it, Fig. 8, indicating severe plastic deformation of the grains prior to the final failure. During the deformation, the lath structure progressively became fragmented into smaller grains which can be observed from the refined microstructure close to the fracture line.

Prior to LCF deformation, the frequency of grains with misorientation angle of $< 2°$ is very low for both the as-built and HIPed conditions; see the four histograms in Fig. 8. By contrast, the overall fraction of grains with misorientation angle between 0° to 5° increases after the LCF deformation. Especially, it seems that the number frequency of grains with misorientation of $< 2°$ increases, suggesting the activity of different slip systems within and across the grains. Grain boundaries with the misorientation angle of $< 2°$ are known as geometrically necessary boundaries (GNBs) which are formed between regions of different strain patterns to accommodate the accompanying difference in lattice

rotation [45]. As the material experiences cyclic loading, the dislocations continuously accumulate until the sources are closed by the back stress associated with the dislocation pile-up [46]. The GNBs may increase to their saturated misorientation value followed by increased activity of grains with $> 2°$ misorientation. Once the LAGBs structure is developed, further strain would be accommodated by gradual rotation of the adjacent grains leading to a continuous increase in misorientation angles [46].

Caution should be taken when considering such low misorientation angle ($< 2°$) distribution statistics since the experimental accuracy for orientation determination by the EBSD commonly does not exceed 1° [47] and the measurement noise can introduce artefacts. This is the reason why only the qualitative distinctions were described by referring to Fig. 8. In general, LCF deformed microstructure is expected to display increased frequency of grain misorientations, implying the increased level of plastic strain or stored energy. Cumulatively, the pattern of local misorientation change is known to be complex and the misorientation angle showing a periodic trend with an increase or decrease in the angle can be expected [46].

Fig. 9 shows the kernel average misorientation (KAM) maps of EBM Ti64 samples before and after LCF deformation. KAM is a measure of local grain misorientation caused by GNDs [48]. The colour scale in the KAM maps represents the intensity of local misorientation, with the maximum set to 5°. Prior to LCF deformation, samples do not exhibit any significant accumulated strain indicating the material was relatively strain-free. The yellow and green colour areas indicate accumulated local strains. Misorientation of grains is an indicator of the dislocation density distribution. The high intensity regions are those where grains deformed and stored energy inside the grains. By contrast, a significantly increased local misorientation was found after LCF deformation due to numerous dislocations generated, see the four KAM maps presented in
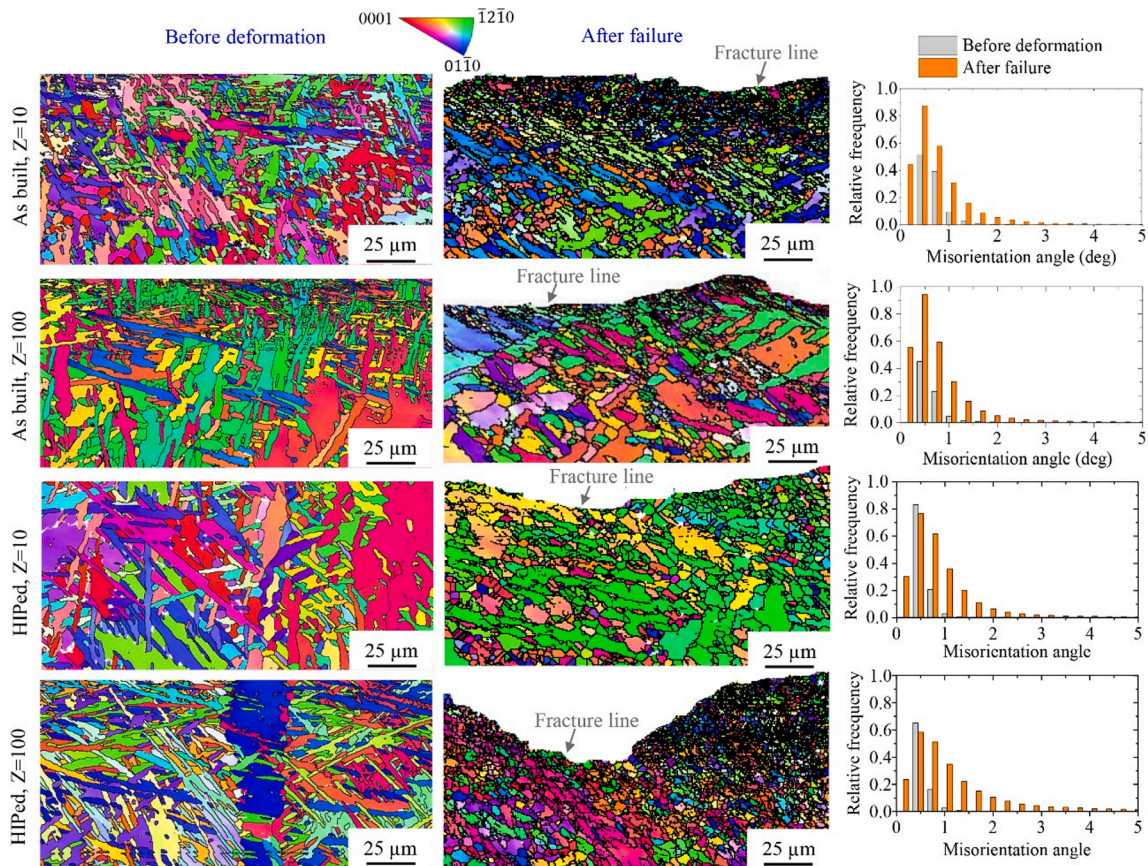
Fig. 8. EBSD IPF-Z orientation maps of α-phase grains before and after the LCF deformation with the top two rows for the as-built condition while the bottom two rows for the HIPed condition. The frequency plots for the misorientation angles between 0° and 5° are also given in the right column.

the right column in Fig. 9.

Close to the fracture surface, it seems that the density of grains with the misorientation angle of $> 2°$ increases, indicating the formation of low-angle grain boundaries (LAGBs with $< 5°$ misorientation) and sub-grain boundaries inside the deformed grains. The presence of high grain misorientation angles at the grain interfaces lead to decreased density and increased misfit stresses resulting in microstructure instability and cracks formation. Although the graded microstructure (Fig. 3e), micro-hardness gradient as well as the graded plastic strain amplitude (Table 2) was found in the as-built condition, no clear evidence of GND gradient can be seen in the KAM maps for $Z = 10$ and 100 samples prior to the LCF deformation. Nevertheless, such a gradient in the local misorientation can be seen in the as-built samples after the deformation to failure, with the $Z = 100$ sample showing higher misorientation density when compared to the $Z = 10$. Compared to the as-built condition, HIPed samples tend to have higher local misorientation density.

3.5. Crack initiation and fracture surfaces

When a material is subjected to cyclic deformation, fatigue crack initiation is often observed either at the surface due to slip bands or in the interior of the specimen associated with defects and inclusions. The scatter in the fatigue life in both the as-built and HIPed samples did not allow any quantitative analysis. However, a closer observation of the results presented in Table 2 reveal that as-built samples have generally higher scatter in fatigue life data compared to the HIPed sample and the mean fatigue life is higher for HIPed sample. To understand the crack initiation mechanism, a detailed SEM fractography was performed.

Fig. 10a to 10d shows the crack initiation sites for the as-built samples. Fatigue cracks tended to initiate either from gas pores or lack-of-fusion defects that are present close to the sample surface. In additive

manufacturing, gas porosity is generally spherical and occurs due to gas trapped in the raw metal powder particles or trapped inert gas during the melting process. By contrast, lack-of-fusion defects are developed due to inappropriate melting conditions leading to process instability, inadequate melting and weak bonding between the layers. Usually they appears as flat band shape with sharp tips. The crack initiation of samples $Z = 10$ and 25 mm is associated with a gas pore close to the sample surface, whereas the crack initiation for samples $Z = 85$ and 100 mm is due to a lack-of-fusion defect present on the surface. Fig. 10e to 10h present the crack initiation sites for the HIPed samples. After HIPing, the fatigue cracks tended to initiate from the sample surface, except for the $Z = 100$ mm sample, where the crack was initiated from a lack-of-fusion defect that was present on the surface, Fig. 10h.

Fig. 11 shows the overall fracture surface together with the enlarged view highlighting the regions of crack initiation, propagation and final failure. The as-built sample condition is shown in Fig. 11a, while the HIPed one is shown in Fig. 11b. Only one sample per condition is shown in Fig. 11 (samples extracted from $Z = 10$ mm) as the remaining samples in the respective condition have similar fatigue fracture mechanisms. The as-built sample consists of a few gas pores and lack-of-fusion defects which are highlighted in Fig. 11a. The spherical gas pores have a mean diameter of 58 ± 10 μm. Gas pores observed on the fracture surface is likely caused by a small bubble of argon trapped inside the powder particles due to the atomization process used to produce the powder. It was also found that the vaporisation of low melting point constituents within the alloy also lead to gas pores in the EBM builds [49]. According to [50], turbulence in the melt pool and a low viscosity liquid metal spattering that ejects away from the melt pool and falls into the molten metal or on the powder bed also leads to gas pores formation.

The presence of lack-of-fusion defects are the direct consequence of the partially melted layer that was formed due to insufficient energy
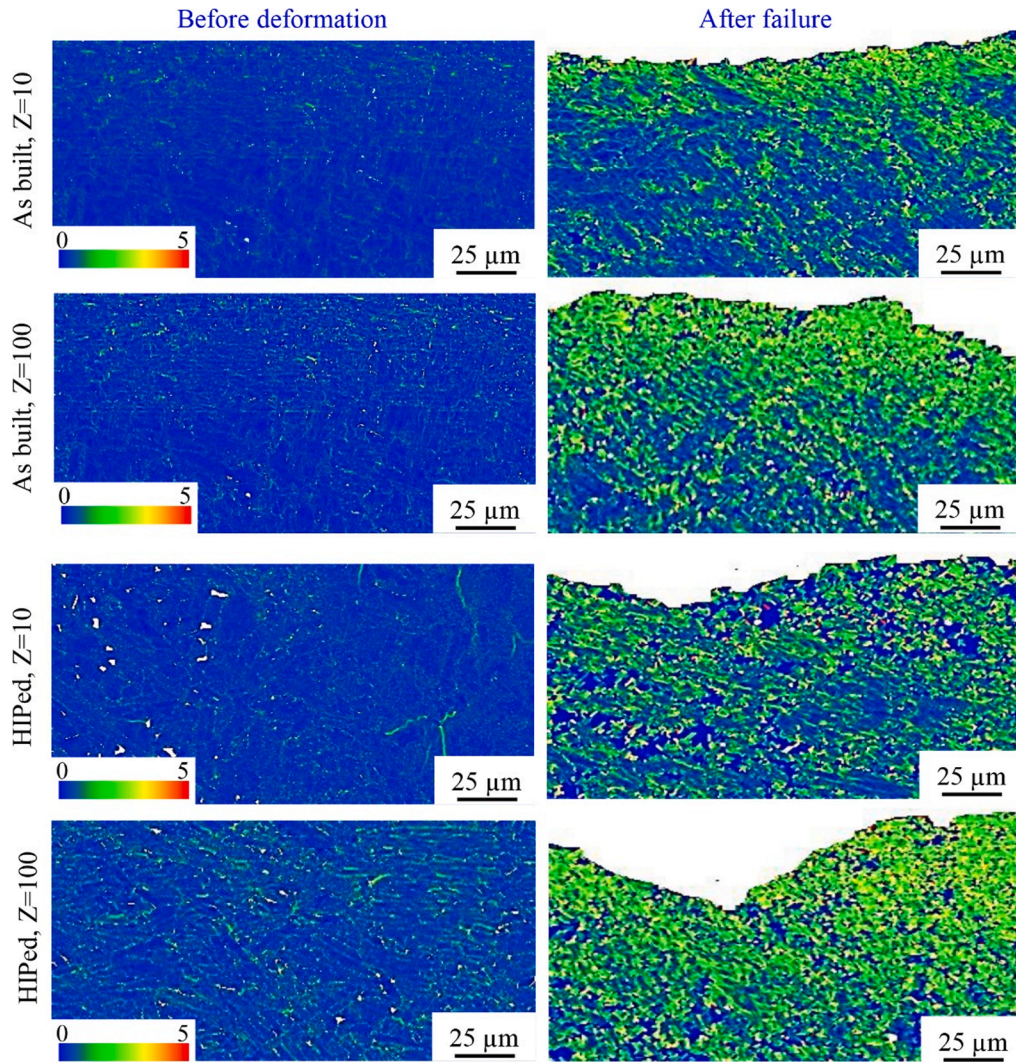
Fig. 9. KAM maps showing the local misorientation distribution before and after the LCF deformation.
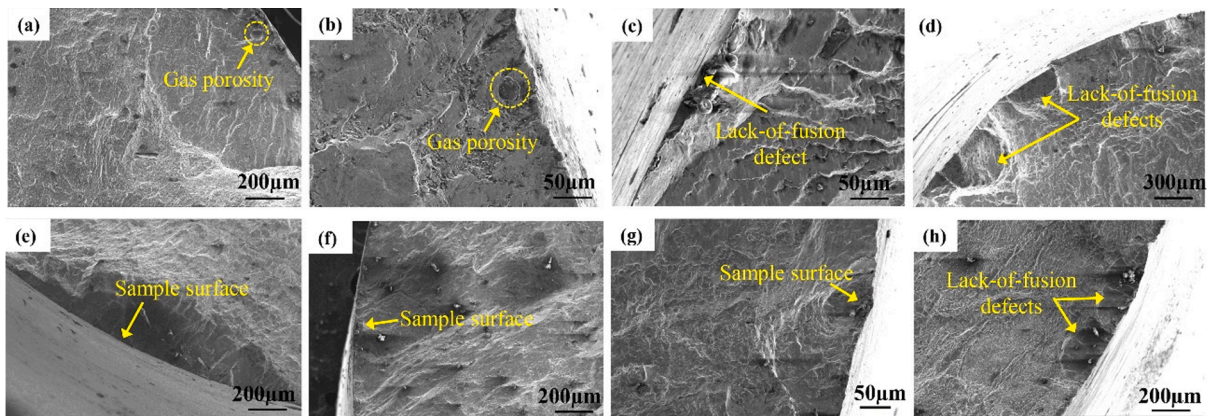

Fig. 10. Fracture surfaces showing crack initiation site: (a) to (d) as-built samples at $Z = 10, 25, 85$ and 100 mm respectively; (e) to (h) HIPed samples, $Z = 10, 25, 85$ and 100 mm respectively. Crack initiation site is highlighted with an arrow.

density during the deposition in that area. The size of the lack-of-fusion defects was measured to be ranging from 100 to 800 μm. The long axis of the lack-of-fusion defect was always found to be within the layer (i.e., X-Y plane that is perpendicular to the Z-build direction). Process induced defects have played a major role in the fatigue performance of the as-built Ti64 samples. Previous studies have shown that the defects

present on or close to the sample surface are more detrimental compared to the defects embedded in the sample due to higher stress concentration associated with the defects on or close to the sample surface [51,52]. Therefore, the large distribution of defects is the governing factor of LCF life in as-built samples. Furthermore, the large variation in the population of the defects seems to explain the large scatter in the total fatigue
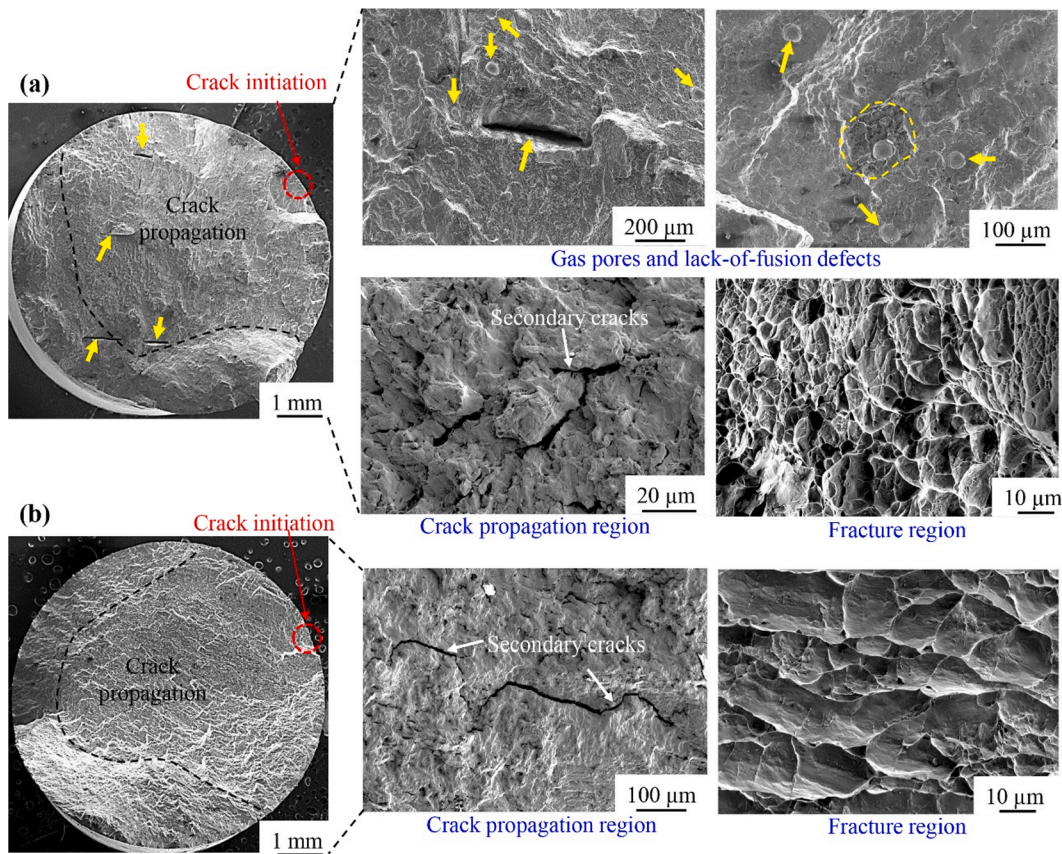
Fig. 11. Fracture surfaces showing the overall and characteristic features: (a) as-built sample at Z = 10 mm; (b) HIPed sample at Z = 10 mm. Crack initiation site is highlighted with red circle. (For interpretation of the references to colour in this figure legend, the reader is referred to the web version of this article.)

life of as-built samples (Table 2).

In the HIPed condition, the overall LCF fatigue life is controlled by the sample surface roughness and the microstructure. The higher fatigue life of HIPed samples is associated with relatively less porosity compared to the as-built samples. Similar observation was made in [24] where the HIPed sample showed higher HCF fatigue life. The occurrence of fatigue crack initiation at the surface is always caused by slip bands located in α and β-phase in Z = 10, 25 and 85 mm samples (Fig. 10e to 10g). Recall that the HIPed sample extracted from Z = 100 (Fig. 10h) failed with the fatigue crack initiated from the lack-of-fusion defects located in the sample surface. This implies that HIPing might not be always successful to fully eliminate these process induced defects. The EBM samples with dimensions of 100 × 15 × 120 mm (Fig. 1a) was subjected to HIPing prior to the fatigue sample extraction and specimen machining. This means that the present case is not indicative of an intrinsic inability of the HIPing process to close surface defects.

The morphology of fracture surfaces in the crack propagation and final failure region is also presented in Fig. 11a and 11b. Secondary cracks can be seen in both the as-built and HIPed conditions, but the length and the number of secondary cracks appear to be higher in the HIPed samples. In Ti64, the α-lath and colony size greatly influence the crack path. The presence of larger α-laths and wider single variant α colonies after HIPing lead to greater crack branching, which might be the reason for the observed large number of secondary cracks. It is apparent that the HIPed samples had a continuous crack branching and bifurcation, involving several secondary cracks growing in parallel to the primary crack. This would also cause a reduction in the effective crack growth driving force of the primary crack and the consequent reduction in the crack growth rate leading to higher fatigue performance. By contrast, the finer α laths and smaller α colonies in the as-built samples lead to less crack branching. In the final fracture region, the fracture surface of both the as-built and HIPed samples is characterised by the dimples indicating ductile fracture. However, finer α laths in the as-built condition results in smaller dimples as revealed in the SEM fractography, whereas coarser α laths in the HIPed samples come with much coarser dimples.

4. Conclusions

The influence of graded microstructure along the build direction of EBM Ti64 on the cyclic plasticity and low-cycle fatigue (LCF) performance is investigated. Both the as-built and HIPed sample conditions are considered. From the detailed microstructure and mechanical data analyses, the following conclusions are drawn.

1. As-built samples have an inhomogeneous microstructure where the α-lath width increases along the build direction. HIPing helps to remove this graded microstructure resulting in a more homogeneous distribution and greater than 50% increase in the α-lath width.
2. Cyclic stress softening during a strain-controlled LCF test can be seen for both the as-built and HIPed conditions. Samples in both the conditions showed cyclic softening behaviour. As-built samples exhibit a graded cyclic softening response where samples from the bottom of the build presents a 2% higher stress amplitude and 38% lower plastic strain range compared to the top. Nevertheless, such difference can be significantly reduced by HIPing.
3. EBSD analysis reveals that the grain misorientation increases after LCF deformation, suggesting that the lath structure progressively become fragmented into smaller grains. As-built samples exhibit comparatively higher intensity of grain misorientation due to smaller α width than the HIPed counterpart.

4. SEM fractography reveals the fatigue crack initiation from gas pores and lack-of-fusion defects in the as-built condition, causing a large scatter in the fatigue life. HIPing helps to reduce the scatter by healing the defects, but there is evidence to show the presence of lack-of-fusion defect in one HIPed sample. A higher number and larger secondary cracks present in the HIPed samples seems to also contribute to the higher fatigue life through the crack branching and bifurcation mechanisms.

Declaration of Competing Interest

The authors declare that they have no known competing financial interests or personal relationships that could have appeared to influence the work reported in this paper.

Data availability

The raw/processed data required to reproduce these findings cannot be shared at this time as the data also forms part of an ongoing study.

References

[1] Yadollahi A, Shamsaei N. Additive manufacturing of fatigue resistant materials: challenges and opportunities. Int J Fatigue 2017;98:14–31. https://doi.org/10.1016/j.ijfatigue.2017.01.001.

[2] Chastand V, Quaegebeur P, Maia W, Charkaluk E. Comparative study of fatigue properties of Ti-6Al-4V specimens built by electron beam melting (EBM) and selective laser melting (SLM). Mater Charact 2018;143:76–81. https://doi.org/10.1016/j.matchar.2018.03.028.

[3] Zhao Z, Zhang F, Dong C, Yang X, Chen B. Initiation and Early-Stage Growth of Internal Fatigue Cracking Under Very-High-Cycle Fatigue Regime at High Temperature. Metall Mater Trans A 2020;51:1575–92. https://doi.org/10.1007/s11661-020-05633-3.

[4] Greitemeier D, Palm F, Syassen F, Melz T. Fatigue performance of additive manufactured TiAl6V4 using electron and laser beam melting. Int J Fatigue 2017; 94:211–7. https://doi.org/10.1016/j.ijfatigue.2016.05.001.

[5] Gu D, Hagedorn YC, Meiners W, Meng G, Batista RJS, Wissenbach K, et al. Densification behavior, microstructure evolution, and wear performance of selective laser melting processed commercially pure titanium. Acta Mater 2012;60: 3849–60. https://doi.org/10.1016/j.actamat.2012.04.006.

[6] Antonysamy AA, Meyer J, Prangnell PB. Effect of build geometry on the β-grain structure and texture in additive manufacture of Ti6Al4V by selective electron beam melting. Mater Charact 2013;84:153–68. https://doi.org/10.1016/j.matchar.2013.07.012.

[7] Gunther J, Krewerth D, Lippmann T, Leuders S, Troster T, Weidner A, et al. Fatigue life of additively manufactured Ti-6Al-4V in the very high cycle fatigue regime. Int J Fatigue 2017;94:236–45. https://doi.org/10.1016/j.ijfatigue.2016.05.018.

[8] Lutjering G, Williams J. Titanium. 2nd ed. Springer-Verlag Berlin Heidelberg; 2007.

[9] Stapleton AM, Raghunathan SL, Bantounas I, Stone HJ, Lindley TC, Dye D. Evolution of lattice strain in Ti–6Al–4V during tensile loading at room temperature. Acta Mater 2008;56:6186–96. https://doi.org/10.1016/j.actamat.2008.08.030.

[10] Lunt D, da Fonseca JQ, Rugg D, Preuss M. Microscopic strain localisation in Ti-6Al-4V during uniaxial tensile loading. Mater Sci Eng A 2017;680:444–53. https://doi.org/10.1016/j.msea.2016.10.099.

[11] Agius D, Kourousis KI, Wallbrink C, Song T. Cyclic plasticity and microstructure of as-built SLM Ti-6Al-4V: The effect of build orientation. Mater Sci Eng A 2017;701: 85–100. https://doi.org/10.1016/j.msea.2017.06.069.

[12] Simonelli M, Tse YY, Tuck C. Effect of the build orientation on the mechanical properties and fracture modes of SLM Ti-6Al-4V. Mater Sci Eng A 2014;616:1–11. https://doi.org/10.1016/j.msea.2014.07.086.

[13] Ren YM, Lin X, Guo PF, Yang HO, Tan H, Chen J, et al. Low cycle fatigue properties of Ti-6Al-4V alloy fabricated by high-power laser directed energy deposition: Experimental and prediction. Int J Fatigue 2019;127:58–73. https://doi.org/10.1016/j.ijfatigue.2019.05.035.

[14] Liu S, Shin YC. Additive manufacturing of Ti6Al4V alloy: a review. Mater Des 2019;164:107552. https://doi.org/10.1016/j.matdes.2018.107552.

[15] Yao Y, Xing C, Peng H, Guo H, Chen B. Solidification microstructure and tensile deformation mechanisms of selective electron beam melted Ni3Al-based alloy at room and elevated temperatures. Mater Sci Eng A 2021;802:140629. https://doi.org/10.1016/j.msea.2020.140629.

[16] Peng H, Shi Y, Gong S, Guo H, Chen B. Microstructure, mechanical properties and cracking behaviour in a γ′-precipitation strengthened nickel-base superalloy fabricated by electron beam melting. Mater Des 2018;159:155–69. https://doi.org/10.1016/J.MATDES.2018.08.054.

[17] Han F, Tang B, Kou H, Li J, Deng Y, Feng Y. Cyclic softening behavior of Ti–6Al–4V alloy at macro and micro-scale. Mater Lett 2016;185:115–8. https://doi.org/10.1016/j.matlet.2016.08.119.

[18] Tan C, Sun Q, Xiao L, Zhao Y, Sun J. Cyclic deformation and microcrack initiation during stress controlled high cycle fatigue of a titanium alloy. Mater Sci Eng A 2018;711:212–22. https://doi.org/10.1016/j.msea.2017.11.019.

[19] Murr LE, Esquivel EV, Quinones SA, Gaytan SM, Lopez MI, Martinez EY, et al. Microstructures and mechanical properties of electron beam-rapid manufactured Ti-6Al-4V biomedical prototypes compared to wrought Ti-6Al-4V. Mater Charact 2009;60:96–105. https://doi.org/10.1016/j.matchar.2008.07.006.

[20] Lu SL, Tang HP, Ning YP, Liu N, StJohn DH, Qian M. Microstructure and mechanical properties of long Ti-6Al-4V rods additively manufactured by selective electron beam melting out of a deep powder bed and the effect of subsequent hot isostatic pressing. Metall Mater Trans A 2015;46:3824–34. https://doi.org/10.1007/s11661-015-2976-3.

[21] Sharma H, Parfitt D, Syed AK, Wimpenny D, Muzangaza E, Baxter G, et al. A critical evaluation of the microstructural gradient along the build direction in electron beam melted Ti-6Al-4V alloy. Mater Sci Eng A 2019;744:182–94. https://doi.org/10.1016/j.msea.2018.12.016.

[22] Tan X, Kok Y, Tan YJ, Descoins M, Mangelinck D, Tor SB, et al. Graded microstructure and mechanical properties of additive manufactured Ti-6Al-4V via electron beam melting. Acta Mater 2015;97:1–16. https://doi.org/10.1016/j.actamat.2015.06.036.

[23] Tan X, Kok Y, Tan YJ, Vastola G, Pei QX, Zhang G, et al. An experimental and simulation study on build thickness dependent microstructure for electron beam melted Ti–6Al–4V. J Alloys Compd 2015;646:303–9. https://doi.org/10.1016/j.jallcom.2015.05.178.

[24] Hrabe N, Gnaupel-Herold T, Quinn T. Fatigue properties of a titanium alloy (Ti-6Al-4V) fabricated via electron beam melting (EBM): effects of internal defects and residual stress. Int J Fatigue 2017;94:202–10. https://doi.org/10.1016/j.ijfatigue.2016.04.022.

[25] Kan W, Chen B, Peng H, Liang Y, Lin J. Formation of columnar lamellar colony grain structure in a high Nb-TiAl alloy by electron beam melting. J Alloys Compd 2019;809:151673. https://doi.org/10.1016/j.jallcom.2019.151673.

[26] ASTM E606, standard Test method for strain-controlled fatigue testing, in: ASTM Int., West Conshohocken, PA, 2021.

[27] Xu H, Ye D, Mei L. A study of the back stress and the friction stress behaviors of Ti-6Al-4V alloy during low cycle fatigue at room temperature. Mater Sci Eng A 2017; 700:530–9. https://doi.org/10.1016/j.msea.2017.06.051.

[28] Guillemer C, Clavel M, Cailletaud G. Cyclic behavior of extruded magnesium: Experimental, microstructural and numerical approach. Int J Plast 2011;27: 2068–84. https://doi.org/10.1016/j.ijplas.2011.06.002.

[29] Galindo-Fernández MA, Mumtaz K, Rivera-Díaz-del-Castillo PEJ, Galindo-Nava EI, Ghadbeigi H. A microstructure sensitive model for deformation of Ti-6Al-4V describing Cast-and-Wrought and Additive Manufacturing morphologies. Mater Des 2018;160:350–62. https://doi.org/10.1016/j.matdes.2018.09.028.

[30] Kuhlmann-Wilsdorf D, Laird C. Dislocation behavior in fatigue II. Friction stress and back stress as inferred from an analysis of hysteresis loops. Mater Sci Eng 1979; 37:111–20. https://doi.org/10.1016/0025-5416(79)90074-0.

[31] Jha JS, Dhala S, Toppo SP, Singh R, Tewari A, Mishra SK, et al. Effect of strain amplitude on low cycle fatigue and microstructure evolution in Ti-6Al-4V: A TKD and TEM characterization. Mater Charact 2019;155:109829. https://doi.org/10.1016/j.matchar.2019.109829.

[32] Dickson JI, Boutin J, Handfield L. A comparison of two simple methods for measuring cyclic internal and effective stresses. Mater Sci Eng 1984;64:L7–11. https://doi.org/10.1016/0025-5416(84)90083-1.

[33] Chen B, Flewitt PEJ, Cocks ACF, Smith DJ. A review of the changes of internal state related to high temperature creep of polycrystalline metals and alloys. Int Mater Rev 2015;60:1–29. https://doi.org/10.1179/1743280414Y.0000000041.

[34] Chen B, Hu JN, Wang YQ, Zhang SY, Van Petegem S, Cocks ACF, et al. Role of the misfit stress between grains in the Bauschinger effect for a polycrystalline material. Acta Mater 2015;85:229–42. https://doi.org/10.1016/j.actamat.2014.11.021.

[35] Shui X, Yamanaka K, Mori M, Nagata Y, Kurita K, Chiba A. Effects of post-processing on cyclic fatigue response of a titanium alloy additively manufactured by electron beam melting. Mater Sci Eng A 2017;680:239–48. https://doi.org/10.1016/j.msea.2016.10.059.

[36] Donachie MJ. Titanium, A technical guide, 2nd edition, ASM International, Metals Park (OH); 2000.

[37] Sun Q, Tan C, Xiao L, Sun J. Effect of size of alpha phases on cyclic deformation and fatigue crack initiation during fatigue of an alpha-beta titanium alloy. MATEC Web Conf 2018;165:15006. https://doi.org/10.1051/matecconf/201816515006.

[38] Gil FJ, Manero JM, Ginebra MP, Planell JA. The effect of cooling rate on the cyclic deformation of β-annealed Ti–6Al–4V. Mater Sci Eng A 2003;349:150–5. https://doi.org/10.1016/S0921-5093(02)00784-0.

[39] DebRoy T, Wei HL, Zuback JS, Mukherjee T, Elmer JW, Milewski JO, et al. Additive manufacturing of metallic components – Process, structure and properties. Prog Mater Sci 2018;92:112–224. https://doi.org/10.1016/j.pmatsci.2017.10.001.

[40] Huang Q, Hu N, Yang X, Zhang R, Feng Q. Microstructure and inclusion of Ti–6Al–4V fabricated by selective laser melting, Front. Mater Sci 2016;10:428–31. https://doi.org/10.1007/s11706-016-0354-8.

[41] Beranger AS, Feaugas X, Clavel M. Low cycle fatigue behavior of an α + β titanium alloy: Ti6246. Mater Sci Eng A 1993;172:31–41. https://doi.org/10.1016/0921-5093(93)90423-C.

[42] Feaugas X, Pilvin PH, Clavel M. Cyclic deformation behaviour of an α/β titanium alloy-II. Internal stresses and micromechanic modelling. Acta Mater 1997;45:2703–14. https://doi.org/10.1016/S1359-6454(96)00407-7.

[43] Luquiau D, Feaugas X, Clavel M. Cyclic softening of the Ti-10V-2Fe-3Al titanium alloy. Mater Sci Eng A 1997;224:146–56. https://doi.org/10.1016/S0921-5093(96)10531-1.

[44] Helbert AL, Feaugas X, Clavel M. Effects of microstructural parameters and back stress on damage mechanisms in α/β titanium alloys. Acta Mater 1998;46:939–51. https://doi.org/10.1016/S1359-6454(97)00288-7.

[45] Hughes DA, Hansen N, Bammann DJ. Geometrically necessary boundaries, incidental dislocation boundaries and geometrically necessary dislocations. Scr Mater 2003;48:147–53. https://doi.org/10.1016/S1359-6462(02)00358-5.

[46] Salishchev G, Mironov S, Zherebtsov S, Belyakov A. Changes in misorientations of grain boundaries in titanium during deformation. Mater Charact 2010;61:732–9. https://doi.org/10.1016/j.matchar.2010.04.005.

[47] Humphreys FJ. Quantitative metallography by electron backscattered diffraction. J Microsc 1999;195:170–85. https://doi.org/10.1046/j.1365-2818.1999.00578.x.

[48] Zhao P-C, Chen B, Zheng Z-G, Guan B, Zhang X-C, Tu S-T. Microstructure and Texture Evolution in a Post-dynamic Recrystallized Titanium During Annealing, Monotonic and Cyclic Loading. Metall Mater Trans A 2021;52:394–412. https://doi.org/10.1007/s11661-020-06071-x.

[49] Gong H, Gu H, Zeng K, Dilip J, Pal D, Stucker B, et al. Melt pool characterization for selective laser melting of Ti-6Al-4V pre-alloyed powder, in: 25th Annu. Int. Solid Free. Fabr. Symp. 2014:256–67.

[50] Gong H, Rafi K, Gu H, Starr T, Stucker B. Analysis of defect generation in Ti-6Al-4V parts made using powder bed fusion additive manufacturing processes. Addit Manuf 2014;1:87–98. https://doi.org/10.1016/j.addma.2014.08.002.

[51] Beretta S, Romano S. A comparison of fatigue strength sensitivity to defects for materials manufactured by AM or traditional processes. Int J Fatigue 2017;94:178–91. https://doi.org/10.1016/j.ijfatigue.2016.06.020.

[52] Biswal R, Zhang X, Syed AK, Awd M, Ding J, Walther F, et al. Criticality of porosity defects on the fatigue performance of wire + arc additive manufactured titanium alloy. Int J Fatigue 2019;122:208–17. https://doi.org/10.1016/J.ijfatigue.2019.01.017.